Molecules and Cells

Research Article

Adherent-to-suspension transition modulates circulating tumor cell dynamics and metastatic potential in melanoma

Dong Ki Lee[1,†], Jongwook Oh[1,2,†], Soyeon Lee[3], Hyunbin D. Huh[4], Yujin Sub[3], Kuhn Yoon[5], Woo Chul Shin[1], Sojin Kim[2], Hyun Woo Park[4,‡,*], and Heon Yung Gee[1,3,6,*,‡]

[1]Department of Pharmacology, Yonsei University College of Medicine, Seoul 03722, Republic of Korea, [2]Department of Dermatology, Severance Hospital, Cutaneous Biology Research Institute, Yonsei University College of Medicine, Seoul 03722, Republic of Korea, [3]Department of Pharmacology, Graduate School of Medical Science, Brain Korea 21 Project, Yonsei University College of Medicine, Seoul 03722, Republic of Korea, [4]Department of Biochemistry, College of Life Science and Biotechnology, Brain Korea 21 Project, Yonsei University, Seoul 03722, Republic of Korea, [5]Yonsei University College of Medicine, Seoul 03722, Republic of Korea, [6]Woo Choo Lee Institute for Precision Drug Development, Seoul 03722, Republic of Korea
*Corresponding authors. hwp003@yonsei.ac.kr (H.W. Park), hygee@yuhs.ac (H.Y. Gee).
https://doi.org/10.1016/j.mocell.2026.100368

ABSTRACT

Melanoma metastasis involves dynamic cellular reprogramming that enables tumor cells to survive detachment and disseminate to distant organs. We investigated the role of adherent-to-suspension transition (AST) in melanoma metastasis, examining its dynamics during metastatic dissemination and its relationship with epithelial-to-mesenchymal-like transition (EMT-like transition). Our findings reveal that AST genes, *IKZF1*, *IRF8*, and *NFE2*, critically modulate anchorage dependence through the regulation of cell adhesion and survival pathways. AST gene expression exhibits dynamic plasticity throughout the metastatic cascade, peaking in circulating tumor cells and reverting in established metastases. Clonal phylogenetic reconstruction reveals that AST-high circulating tumor cell clones possess enhanced metastatic capacity and dominate distant lesions. Notably, AST enhances metastatic capabilities and invasiveness in melanoma independently of EMT-like transition. Spatial analysis further indicated that AST-positive tumor cells preferentially localize near blood vessels, suggesting a facilitating role in blood-borne metastasis. These findings provide new insights into the mechanisms driving melanoma metastasis and highlight AST as a key factor contributing to tumor cell plasticity and dissemination.

Keywords: Adherent-to-suspension transition, Anchorage dependence, Circulating tumor cell, Melanoma, Metastasis

BACKGROUND

Metastasis, the dissemination of cancer cells to organs distant from where they originate, is the main barrier to effective cancer treatment and the leading cause of cancer-related mortality (Gerstberger et al., 2023; Siegel et al., 2024). This process encompasses a series of biological events, including local invasion of cancer cells at the primary site, entry into the bloodstream, survival within the circulatory system, exit from the bloodstream into adjacent tissues, and colonization and proliferation at a new site (Lin et al., 2021). Although primary tumors can often be cured with local therapies such as surgery and radiation, metastatic cancer is a systemic disease affecting multiple organs, culminating in the death of the patient (Gerstberger et al., 2023; Massagué and Ganesh, 2021).

Melanoma presents formidable therapeutic challenges due to its propensity for metastasis. In early-stage melanoma, when the cancer is confined to its primary site, surgical resection offers high cure rates, with a 5-year survival rate exceeding 99% (Saginala et al., 2021). However, the prognosis drastically changes once melanoma metastasizes to distant organs, as its resistance to available therapies reduces the 5-year survival rate to approximately 30% (Saginala et al., 2021). Hence, elucidating the underlying mechanisms of melanoma metastasis is crucial for advancing melanoma treatment strategies.

Circulating tumor cells (CTCs) are essential precursors of metastasis (Ring et al., 2023). CTCs participate in the intermediate phases of the metastatic cascade. Recent technological advancements have enabled the detection and isolation of these rare CTCs (Nagrath et al., 2007; Zhang et al., 2023). Studies have revealed the unique biological characteristics of CTCs, including the presence of CTC clusters and their interaction with the immune system (Aceto et al., 2014; Szczerba et al., 2019). However, the mechanism by which CTCs originate and detach from the primary tumor needs further clarification.

† Dong Ki Lee and Jongwook Oh contributed equally to this work.
‡ These authors jointly supervised this work.

eISSN: 1016-8478

The epithelial-to-mesenchymal transition (EMT) involves a transformation whereby epithelial cells lose their characteristic adhesion and polarity, adopting traits that enable migration and invasion, contributing to the ability of cancer cells to invade, metastasize, develop resistance to drugs, and maintain stemness and plasticity (Bakir et al., 2020; Nieto et al., 2016). Although melanoma originates from neural crest-derived cells and not epithelial tissues, accumulating evidence indicates that melanoma cells can undergo an EMT-like transition—acquiring mesenchymal-like features that enhance metastatic potential and therapeutic resistance (Müller et al., 2014; Pedri et al., 2022; Vandamme et al., 2020). However, because both epithelial and mesenchymal phenotypes are typically associated with adherent cell types, additional mechanisms may be needed to enable tumor cells to adopt a suspension-compatible state. This raises the possibility of a distinct reprogramming process that confers anchorage independence, facilitating intravasation and survival in the circulation.

Recent studies have demonstrated a distinct transcriptional program termed adherent-to-suspension transition (AST), in which a combination of specific hematopoietic transcriptional regulators reprogram the anchorage dependence of cancer cells (Huh et al., 2024; Huh et al., 2023; Lee et al., 2024a). The AST signature was systematically derived from a meta-analysis of transcriptomic data across adherent and suspension cells lines from public databases. From an initial pool of candidate differentially expressed genes, functional screening identified a core set of factors, *IKZF1*, *IRF8*, *NFE2*, and *BTG2*, capable of autonomously reprogramming tumor cells to survive and proliferate in suspension (Huh et al., 2024). In this study, we explore the role of AST in melanoma metastasis, focusing on the regulatory role of these transcription factors in facilitating metastatic dissemination.

MATERIALS AND METHODS

Cell Lines and Cell Culture

Cells were maintained in a humidified incubator at 5% CO_2 and 37°C. HEK293T (ATCC, CRL-3216), SK-MEL-28 (ATCC, HTB-72), IGR1 (AcceGen, ABC-TC537S), A375 iRFP (Imanis Life Sciences, CL089), and B16F10 GFP cells (Imanis Life Sciences, CL068) were cultured in Dulbecco's Modified Eagle Medium (Capricorn Scientific, DMEM-HXA, Germany) supplemented with 10% fetal bovine serum (FBS, HyClone, Cytiva, SV30207.02, MA, USA) and 1% penicillin/streptomycin (Invitrogen, Thermo Fisher Scientific, 15140122, MA, USA). G-361 cells (ATCC, CRL-1424) were cultured in McCoy's Media (Gibco, Thermo Fisher Scientific, 16600082) supplemented with 10% FBS and 1% penicillin/streptomycin. No cell lines used in this study were found in the databases of commonly misidentified cell lines maintained by the International Cell Line Authentication Committee and NCBI BioSample. All cell lines were tested and confirmed to be mycoplasma-free.

Viral Infection

HEK293T cells were transfected with pMD2G (Addgene, plasmid 12259) and psPAX2 plasmids (Addgene, plasmid 12260), along with constructs cloned into a lentiviral vector (Addgene, plasmid 107505), using the Lipofectamine 2000 Transfection Reagent (Invitrogen, 11668019), according to the manufacturer's protocol. Media containing viral particles were harvested at 48 h post transfection, passed through a 0.45-μm filter (Corning, 431220, NY, USA), supplemented with 8 μg/mL polybrene (Sigma-Aldrich, TR-1003-G, Germany), and used for infection. At 24 h after infection, the transduced cells were incubated with fresh medium for another 24 h and selected using puromycin (Gibco, A1113803).

Establishment of Doxycycline-Inducible B16F10-3AST^{TetR} Cells and Assessment of Anchorage Plasticity

To establish a doxycycline-inducible B16F10-3AST^{TetR} melanoma cell line, B16F10 cells were transduced with lentiviral constructs encoding the AST genes (*IKZF1*, *IRF8*, and *NFE2*) under the control of a tetracycline response element promoter. Following transduction, single-cell clones were isolated and expanded. Inducible AST gene expression was validated by Western blot analysis after treating the cells with 100 ng/mL doxycycline for 48 h.

To investigate the plasticity of AST-driven anchorage independence, B16F10-3AST^{TetR} cells underwent repeated cycles of doxycycline induction and withdrawal. Cells were treated with 100 ng/mL doxycycline for 48 h, and detachment was monitored. After withdrawal, cells were cultured in doxycycline-free medium to assess their ability to reattach and revert to an adherent phenotype.

Orthotopic Mouse Model Experiments

All animal experimental protocols were reviewed and approved by the Yonsei University Institutional Animal Care and Use Committee (approval number 2021-0127, 2021-0302, and 2023-0185). All mice were handled in accordance with the Guidelines for the Care and Use of Laboratory Animals. NOD/Shi-scid IL2 receptor gamma-null (NOG) mice were purchased from KOATECH, Inc (South Korea). For the A375 cell footpad implantation model, 1×10^7 iRFP-positive A375 melanoma cells were subcutaneously implanted into the footpads of 5-week-old male mice ($N = 8$). NOG mice used in these experiments had identical genotypes and genetic backgrounds. C57BL/6 N mice were purchased from Orient Bio Inc. (South Korea). For the B16F10 cell footpad implantation model, 5×10^5 GFP-positive B16F10 melanoma cells were subcutaneously implanted into the footpads of 7-week-old male mice ($N = 8$). The tumor size did not exceed the maximal tumor volume limit, which was 2 cm^3, in this study.

Melanoma Primary Tumor and Lung Metastasis Tissue Dissociation

iRFP-positive A375 and GFP-positive B16F10 cells were isolated from primary tumor sites and the lungs. Primary tumor and metastasized lung tissues were digested in 5 mL of enzyme buffer containing 0.2 mg/mL collagenase type II (Worthington, LS004174, NJ, USA), 0.1 mg/mL DNase I (Roche, 11284932001, Germany), and 0.8 mg/mL dispase (Gibco, 17105041) at 37°C for 45 min. After complete digestion, the resulting cell suspension was filtered through a 40-μm cell strainer and washed with phosphate-buffered saline (PBS). Red

blood cell lysis was then performed using the ACK lysis buffer (Gibco, A1049201) for 5 min at 25°C.

Cell Sorting Strategy

For melanoma cell isolation, fluorescence-activated cell sorting (FACS) was performed to enrich for iRFP-positive melanoma cells. Single-cell suspensions were prepared from tumor tissues and stained with an anti-mouse CD45 antibody conjugated to FITC (Miltenyi Biotec, 130-116-500, Germany) to exclude immune cells. Cells were sorted based on Alexa Fluor 700 fluorescence to identify iRFP-positive populations while gating out GFP-positive cells to ensure the exclusion of nonmelanoma and immune cell populations. Sorting was conducted using a BD FACSAria cell sorter (BD Biosciences, CA, USA), and data were analyzed using the FlowJo software (v10.8, BD Biosciences, OR, USA). Only iRFP-positive and GFP-negative melanoma cells were collected for downstream applications.

Generation of Single-Cell RNA Sequencing Data From Orthotopic Mouse Models

For the A375-derived orthotopic mouse model, single-cell RNA sequencing (scRNA-seq) libraries were created using the Chromium Next GEM Single-Cell 3' RNA library v3.1 (10x Genomics, CA, USA) with a target of 10,000 cells per library according to the manufacturer's suggestions. For both the A375 and B16F10 orthotopic models, a pooling strategy was used in which samples from $N = 8$ mice were combined for each condition (primary, CTC, and metastasis) prior to single-cell library preparation. This approach was necessary to obtain sufficient numbers of rare CTCs, as individual mice typically yield too few CTCs for robust scRNA-seq profiling using the 10x Genomics platform. This droplet-based system uses barcodes (one for each cell) and unique molecular identifiers (UMIs, one for each unique transcript) to obtain a unique 3′-mRNA gene expression profile from every captured cell. All samples were sequenced on an Illumina HiSeq X Ten (Illumina, CA, USA).

scRNA-seq Analysis of Primary Tumor Cells, CTCs, and Metastatic Tumor Cells

The Illumina outputs of A375-derived and B16F10-derived mouse samples were mapped to the human (GRCh38) and mouse (GRCm38/mm10) reference genomes, respectively, using Cell Ranger 7.0.0 (10x Genomics). Gene-wise read counts for genes with at least 500 reads were exported from Cell Ranger to the Matrix Market format and imported into R using Seurat's Read10X function. Prior to quality control, the A375-derived dataset consisted of 13,724 primary tumor cells, 9,697 CTCs, and 6,541 metastatic tumor cells, while the B16F10-derived dataset contained 1,084 primary tumor cells, 1,278 CTCs, and 1,743 metastatic tumor cells. Quality control was performed separately for each library (Kim et al., 2024). Cells were filtered based on the following criteria: (i) gene detection (nFeature_RNA) between 500 and 10,000; (ii) total UMIs (nCount_RNA) less than 100,000; and (iii) mitochondrial gene content less than 20% of total reads. Potential doublets were identified and removed using DoubletFinder (v3.0) with an expected doublet rate of 7.5% and optimal pK values determined via parameter sweep (paramSweep_v3). To restrict analyses to tumor populations, cells expressing the leukocyte marker *PTPRC* (CD45) were excluded. After quality filtering, 19,419 cells from the A375-derived model (11,899 primary tumor cells, 2,838 CTCs, and 4,682 metastatic tumor cells) and 2,988 cells from the B16F10-derived model (882 primary tumor cells, 883 CTCs, and 1,223 metastatic tumor cells) were subjected to further analysis.

Statistical analyses of the 10x data were conducted using the Seurat software package (v4.4.0) for R (Karras et al., 2022). Data normalization and scaling were performed using SCTransform (Seurat v4.4.0), with mitochondrial percentage regressed out to minimize technical variance. For integration, the top 3,000 highly variable genes were identified using the vst method. Following principal component analysis (PCA) on the SCT-normalized assay, biological samples were harmonized using Harmony (v0.1.1) with the original identity variable as a grouping factor to mitigate batch effects. Dimensionality reduction and clustering were conducted using the first 30 principal components (PCs 1-30), as determined by elbow plot analysis. Cell clusters were identified using the Louvain algorithm with a resolution of 1.0. Final visualization was performed using Uniform Manifold Approximation and Projection (UMAP) with a random seed of 1,000 to ensure reproducibility.

Copy Number Variation (CNV)-Based Clonal Inference With Numbat

To resolve the subclonal architecture and evolutionary dynamics of tumor cells across primary, CTC, and metastatic compartments, we performed single-cell copy number variation (CNV) analysis using Numbat (v1.3.0) (Gao et al., 2023). Raw gene-wise read counts were processed using the numbat pipeline. Allele-specific expression was extracted by mapping reads to a reference panel of common SNPs (1000 Genomes Project) using cellsnp-lite. Genomic regions of copy-neutrality were automatically identified to establish a baseline for each sample. Numbat integrated chromosomal gene expression (HMM-based) and B-allele frequency (BAF) data to identify large-scale deletions, amplifications, and losses of heterozygosity (LOH). Cells were assigned to subclones based on their posterior probability of harboring specific CNV events. A consensus clonal phylogeny was constructed using a minimum-spanning tree approach. To ensure robustness, parameter sweeps were conducted on the maximum number of iterations and the smoothing window size. Only cells with a high-confidence assignment (posterior probability > 0.95) were retained for subclonal proportion analysis. Clonal assignment remained stable across varying levels of transcriptome coverage, confirming that the inferred architecture was not an artifact of sequencing depth.

Trajectory Inference and Pseudotime Analysis

To model the transcriptional dynamics of the AST, we performed trajectory inference on the scRNA-seq data from the A375- and B16F10-derived mouse model using the Monocle 3 R package (v1.3.1) (Cao et al., 2019; Qiu et al., 2017; Trapnell et al., 2014). Dimensionality reduction was performed using UMAP, and the principal graph was learned with default parameters. To establish a biologically relevant directionality for the "AST-priming"

continuum, we designated the trajectory root by identifying the cell cluster with the lowest aggregate expression of the AST genes. Pseudotime was subsequently calculated with the starting point anchored at the predefined root. We visualized the expression kinetics of AST-associated genes, EMT-like markers, and MET-like markers along the pseudotime axis. Co-expression patterns and gene expression dynamics were analyzed to determine the coordination of the AST program relative to classical epithelial-mesenchymal transition pathways.

Xenium *In Situ* Analysis

Formalin-fixed, paraffin-embedded primary tumor samples from the B16F10 mouse model ($n = 3$) were used for the Xenium *in situ* analysis. The Xenium Prime 5 K Mouse Pan Tissue & Pathways Panel (10x Genomics) was employed following the manufacturer's standard workflow. Data generated from the Xenium platform were processed using the Seurat software package (v4.4.0) in R for downstream analysis. Quality control was performed by removing cells with zero detected Xenium counts (nCount_Xenium = 0) and excluding low-complexity cells with fewer than 50 detected genes (nFeature_Xenium ≤ 50). Counts were normalized and variance-stabilized using the SCTransform workflow to account for differences in capture efficiency and technical variation across cells. Dimensionality reduction was performed using PCA (30 components), and a UMAP embedding was generated using the first 30 PCs. A k–nearest neighbor graph was constructed on the PCA space (dims 1–30), followed by graph-based clustering using Louvain community detection at a resolution of 0.8.

Cell-type annotation was performed by integrating automated reference-based prediction and canonical marker validation. First, clusters were annotated using scCATCH with the mouse tissue-specific cell taxonomy reference database (CellMatch), using the reference marker sets corresponding to skin, subcutaneous tissue, and blood. Melanoma tumor cells were identified based on expression of melanocytic markers (*Tyrp1*, *Sox10*, and *Cspg4*). AST-positive tumor cells were defined by elevated expression of the AST genes (*IKZF1*, *IRF8*, and *NFE2*), allowing classification into AST-positive and AST-negative tumor states.

AST-positive tumor cells were identified based on the expression of the *Ikzf1*, *Irf8*, and *Nfe2* marker genes. EMT-like transitioned tumor cells were annotated according to the expression of *Axl*, *Cdh2*, and *Zeb1*, whereas MET-like transitioned cells were identified based on the expression of *Mitf*, *Cdh1*, and *Zeb2*. All tumor cells were confirmed to be negative for immune cell markers, such as *Cd4*, *Cd8a*, and *Ptprc*, to ensure the exclusion of immune cell populations. Blood vessels were identified using a binary expression threshold, defined by the expression of one or more endothelial cell markers, specifically *Pecam1* and *Cd34*. Intercellular distances were computed as Euclidean distances using the x- and y-coordinates extracted in R. Distance of different cell states was calculated based on the nearest distance to each blood vessel.

Visium Analysis

The SpaceRanger output of the melanoma sample was further analyzed using the Seurat spatial vignette. In brief, spots were retained when nFeature_Spatial > 1,000 and percent.mt < 5% and expression data were normalized using SCTransform. We performed manual grid alignment using the Loupe Browser. For cell-type probability calculations, the probability of a single bin50 matching a specific cell type was measured using the AUCell package with default parameters. Blood vessels were identified using a binary expression threshold defined by the expression of one or more endothelial cell markers, specifically Pecam1 and Cd34. Euclidean distances between cell types were measured. Cell-cell interaction analysis was performed using the CellChat package (v2.1.0).

Immunocytochemistry of AST Proteins

For immunofluorescence staining, primary tumors were fixed in 4% paraformaldehyde overnight, paraffin-embedded, and sectioned. Paraffin-embedded sections of primary tumors were rehydrated through a series of xylene and graded alcohol solutions and washed with PBS (Park et al., 2025). The samples were permeabilized with 0.15% Triton X-100 in PBS and blocked with 5% goat serum in PBS. Cells were then incubated at 4°C overnight with the following primary antibodies at 1:100 dilutions: anti-Ikzf1 (clone D6N9Y, Cell Signaling Technology, 14859, MA, USA), anti-CD31 (clone TLD-3A12, Thermo Fisher Scientific, MA1-81051), anti-hemoglobin A (Proteintech, 14537-1-AP, IL, USA), and anti-GFP (Abcam, ab13970, UK). After several washes, the samples were incubated with the respective secondary antibodies for 1 h at 25°C. The samples were then mounted with a fluorescence mounting medium (Dako, Agilent Technologies, CA, USA), and immunofluorescent images were acquired under an LSM700 or LSM780 confocal microscope (Carl Zeiss, Germany).

Dissemination Assay

Dissemination assay was performed using B16F10, A375, SK-MEL-28, IGR, and G-361 cells, with each cell line cultured in its own respective growth media. For the assay, cells were seeded at low density and cultured until reaching 100% confluence. After an additional 72-h incubation without media change, spontaneously detached CTC-like cells were harvested. These CTC-like cells were reseeded and found to reattach and form metastasis-like colonies, mimicking the metastatic cascade.

Annexin V/PI Staining for Flow Cytometry

To assess cell viability and apoptosis in the dissemination assay, Annexin V-FITC and Propidium Iodide (PI) staining was performed using the Dead Cell Apoptosis Kit (Invitrogen, Thermo Fisher Scientific, V13242) according to the manufacturer's instructions. Briefly, cells were harvested, washed twice with cold PBS, and resuspended in 1× Annexin V binding buffer. Cells were incubated with Annexin V-FITC and PI for 15 min at room temperature in the dark and analyzed immediately by flow cytometry.

Debris was excluded based on forward- and side-scatter gating, and doublets were removed using FSC-W versus FSC-H parameters. Compensation was established using single-stained controls. Data were analyzed using FlowJo software (v10.8). Cells were classified as viable (Annexin V^-/PI^-), early apoptotic (Annexin V^+/PI^-), late apoptotic/secondary necrotic

(Annexin V^+/PI^+), or necrotic (Annexin V^-/PI^+), and population percentages were quantified.

RNA Sequencing and Data Analysis

For transcriptomic analysis, 3 biological replicates were prepared for each experimental condition. Total RNA was extracted using TRI reagent, and 1 μg of RNA was used for cDNA library preparation with the TruSeq Stranded mRNA Sample Prep Kit (Illumina) following the manufacturer's protocol (TruSeq Standard mRNA Sample Preparation Guide, Part #15031047 Rev. E). Library quality and size distribution were assessed using an Agilent 2100 Bioanalyzer with a DNA 1000 chip, and samples were normalized to 2 nM before sequencing. RNA sequencing was performed using NovaSeqX (Illumina). Sequence reads were processed and assembled using the CLC Main Workbench Software package (version 21.0.1). Differential gene expression analysis was conducted using the DESeq2 R package (Love et al., 2014), and statistical significance was determined based on adjusted p-values (Lee et al., 2024b).

For PCA, variance-stabilizing transformation was applied to RNA-seq data. Principal components (PC1 and PC2) were calculated based on the 500 most variable genes using DESeq2 R package (Love et al., 2014). Gene set enrichment analysis (GSEA) was performed in preranked mode using the GSEA software v4.3.2 (Subramanian et al., 2005), with default parameters. Normalized enrichment score (NES) with corresponding *P* values is presented in the GSEA plots.

Quantitative Real-Time PCR

Cells were harvested for RNA extraction using the Hybrid-R kit (GeneAll, 305-101, South Korea). RNA samples were reverse-transcribed to complementary DNA using the RNA-to-cDNA EcoDry Premix (Clontech, Takara Bio USA, 639549, CA, USA). qPCR was performed using the TB Green Premix Ex Taq kit (Takara Bio, RR420B, Japan) with QuantStudio 3 (Applied Biosystems, MA, USA) (Bong et al., 2024). The following primers were used for qPCR: *IKZF1*, 5′-TTTCAGGGAAGGAAAG CCCC-3′ (forward) and 5′-CTCCGCACATTCTTCCCCAT-3′ (reverse); *IRF8*, 5′-AGCATGTTCCGGATCCCTTG-3′ (forward) and 5′-CGGTCCGTCACTTCCTCAAA-3′ (reverse); *NFE2*, 5′-ACAGCTGTCCACTTCAGAGC-3′ (forward) and 5′-TGAGC AGGGGCAGTAAGTTG-3′ (reverse); *GAPDH*, 5′-GTCTCCTCT GACTTCAACAGCG-3′ (forward) and 5′-ACCACCCTGTTGCT GTAGCCAA-3′ (reverse) for human cell lines; *Ikzf1* 5′-CCACA ACGAGATGGCAGAAGAC-3′ (forward) and 5′-GGCATGTCTG ACAGGCACTT-GT-3′ (reverse); *Irf8* 5′-CAATCAGGAGGTGG ATGCTTCC-3′ (forward) and 5′-GTTCAGAGCACAGCGTAAC CTC-3′ (reverse); *Nfe2* 5′-GGAGAGATGGAACTGACTTG-GC-3′ (forward) and 5′-GCAATATGTTGGAGGTGGCAGTG-3′ (reverse); *Gapdh*, 5′-CATCACTGCCACCCAGAAGACTG-3′ (forward) and 5′-ATGCCAGTGAGCTTCCCGTT-CAG-3′ (reverse) for mouse cell lines.

Statistical Analysis

All quantitative data were obtained from at least 3 independent biological replicates. Data are presented as the mean ± standard deviation unless otherwise noted in the Figure legends. Statistical differences between 2 groups were examined using a 2-tailed, unpaired Student's *t*-test and one-way analysis of variance with Bonferroni correction for multiple comparisons. Statistical tests were performed using the GraphPad Prism 8.0 software (GraphPad Software, CA, USA). Unless otherwise specified, all quantitative data are presented as mean ± standard deviation (SD). For in vitro assays, *N* represents the number of independent biological replicates. For in vivo studies, *N* indicates the number of individual mice per group. Statistical significance was determined using 2-tailed unpaired Student's *t*-tests for 2-group comparisons, or one-way ANOVA followed by Bonferroni's post hoc test for multiple comparisons. Non–normally distributed data, such as cell-to-vessel distances, were analyzed using the Wilcoxon rank-sum test. Two-sided *P* values < 0.05 were considered significant. No statistical methods were used for sample size determination. The sample size was based on previous experience with experimental variability.

RESULTS

AST Genes Are Enriched in CTCs Across Multiple Models

Melanoma metastasis involves a complex process of cellular reprogramming that enables tumor cells to transit between adherent and suspension states. To investigate the changes in AST factors during metastasis, we employed an orthotopic mouse model using near-infrared fluorescent protein (iRFP)-expressing A375 melanoma cells harboring the BRAF V600E mutation (Fig. 1A). We conducted transcriptomic analysis across 3 distinct stages of hematogenous melanoma dissemination: primary tumors, CTCs from whole blood, and metastatic tumors (Supplementary Fig. S1A). To ensure the purity of melanoma cells, we first isolated iRFP-positive and CD45-negative melanoma cells using FACS, followed by scRNA-seq, which revealed that the majority of cells expressed melanocyte markers (Supplementary Fig. S1B, C). After cell filtering using quality control measures and correcting for batch effects, we visualized the sequencing data from 11,899 primary tumor cells, 2,838 CTCs, and 4,682 metastatic tumor cells using UMAP (Fig. 1B). Given the unique ability of CTCs to survive and propagate within the bloodstream, we hypothesized that the transcriptional profiles of CTCs would differ from those of primary and metastatic tumor cells. Accordingly, UMAP clustering revealed that while some overlap existed, CTCs formed distinct clusters distinguished from primary and metastatic tumor cells (Fig. 1B). These findings indicate the transcriptional reprogramming that occurs during melanoma dissemination.

In our previous study, we identified the induction of AST genes during CTC dissemination, followed by a subsequent reduction in their levels in colonized lung nodules, suggesting reversible gene expression plasticity (Huh et al., 2023). Mechanistically, AST was characterized by 2 key processes: first, the spontaneous dissociation of cells from the extracellular matrix (ECM), driven by the suppression of the YAP/TEAD pathway, leading to decreased expression of ECM-integrin genes; and second, the acquisition of anoikis resistance facilitated by the activation of hemoglobin genes (Huh et al., 2023). Consistently, the expression levels of *IKZF1*, *IRF8*, and *NFE2* were significantly elevated in CTCs compared with

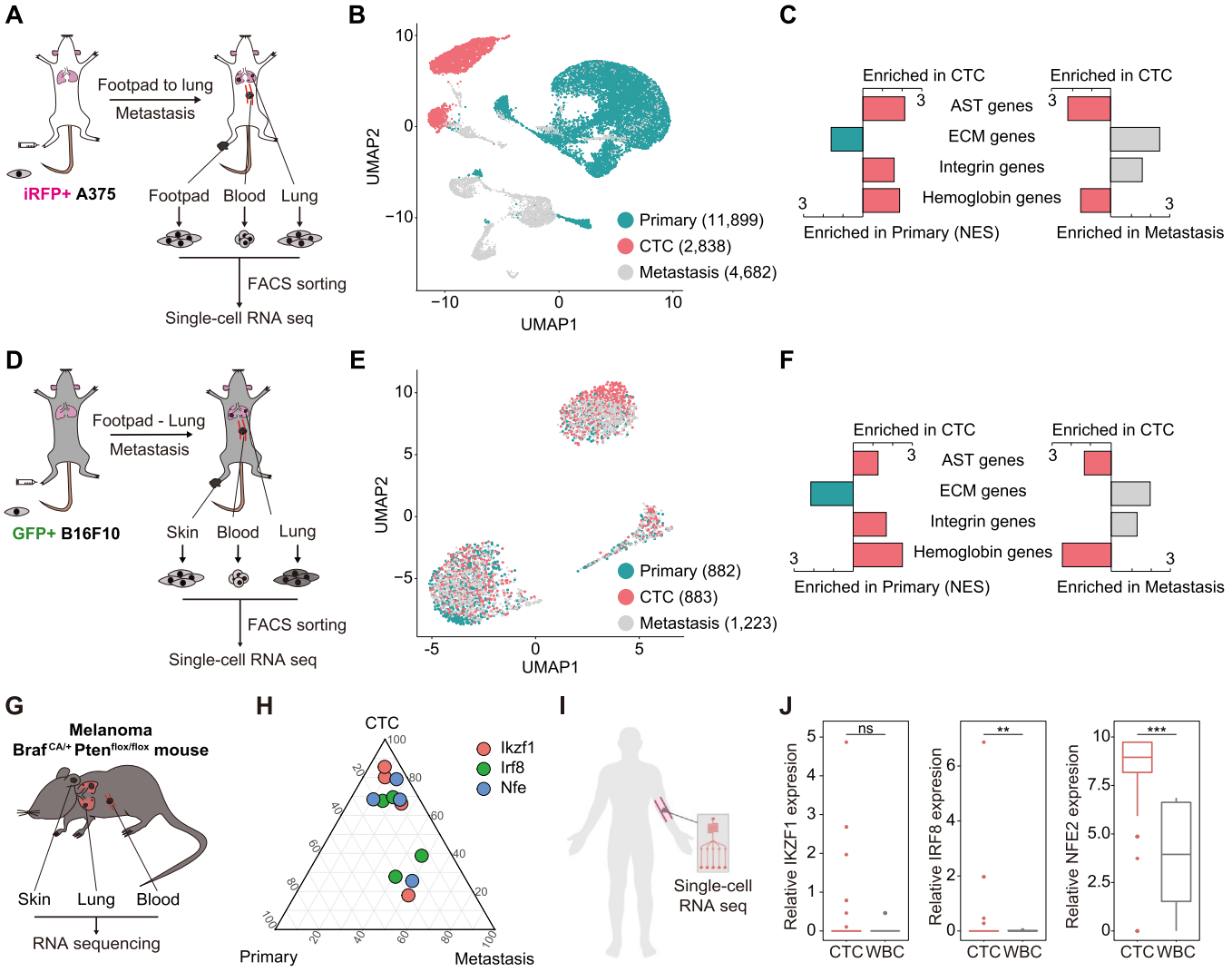

Fig. 1. *Induction of adherent-to-suspension transition (AST) genes in disseminated circulating tumor cells.* (A) Schematic representation of the isolation and single-cell RNA sequencing (scRNA-seq) analysis of A375-derived primary, circulating (CTCs), and metastatic tumor cells pooled from $N = 8$ mice of the orthotopic melanoma metastasis model. iRFP-positive A375 melanoma cells were injected into the footpads of NOG mice, and tumor cells were subsequently isolated using fluorescence-activated cell sorting (FACS) for transcriptomic analysis. (B) UMAP representation of the analyzed transcriptomes of 11,899 primary tumor cells (blue), 2,838 CTCs (red), and 4,682 metastatic tumor cells (gray). (C) Gene set enrichment analysis (GSEA) revealing the relative upregulation in the expression of AST, extracellular matrix (ECM), integrin-related, and hemoglobin genes in A375-derived primary tumor cells, CTCs, and metastatic tumor cells. The expression of AST and hemoglobin genes was upregulated in CTCs, whereas that of ECM genes was downregulated. (D) Schematic representation of the isolation and scRNA-seq analysis of B16F10-derived primary tumor cells, CTCs, and metastatic tumor cells pooled from $N = 8$ mice of the orthotopic melanoma metastasis model. GFP-positive B16F10 melanoma cells were injected into the footpads of C57BL/6N mice, and tumor cells were isolated using FACS for transcriptomic analysis. (E) UMAP embedding of single-cell transcriptomic profiles from 882 primary tumor cells (blue), 883 CTCs (red), and 1,223 metastatic tumor cells (gray), demonstrating distinct cellular populations in the B16F10-derived model. (F) Bar plot displaying GSEA results for AST, ECM, integrin, and hemoglobin genes among B16F10-derived primary tumor cells, CTCs, and lung metastatic tumor cells. (G) Schematic representation of the inducible BRAF-PTEN-driven melanoma mouse model (GSE52031). (H) Ternary plot illustrating AST gene expression in paired primary tumors, CTCs, and lung metastatic tumors. (**I**) Representation of the workflow for isolating CTCs and performing scRNA-seq from metastatic melanoma patients (GSE157745). (**J**) Boxplots depicting the relative expression levels of *IKZF1*, *NFE2*, and *IRF8* in CTCs compared with white blood cells from metastatic melanoma patients. AST gene expression was elevated in CTCs, with statistical significance values of $P = 0.15$ (*IKZF1*), $P = 1.6 \times 10^{-3}$ (*IRF8*), and $P = 2.5 \times 10^{-4}$ (*NFE2*), respectively. AST, adherent-to-suspension transition; CTC, circulating tumor cell; ECM, extracellular matrix; FACS, fluorescence-activated cell sorting.

primary tumor cells but reverted to baseline levels in metastatic tumor cells (Supplementary Fig. S1D, E). Further analysis revealed a marked upregulation of hemoglobin genes in CTCs, while ECM genes were downregulated, reinforcing the role of AST in facilitating cellular detachment and survival in circulation. These trends were reversed upon metastatic colonization,

underscoring the dynamic and reversible nature of AST during the metastatic cascade (Fig. 1C). Collectively, these findings emphasize the critical role of AST plasticity in tumor cell detachment, circulation, and reattachment, highlighting its contribution to melanoma dissemination.

To further investigate the plasticity of AST, we utilized a syngeneic mouse model of melanoma with green fluorescent protein (GFP)-labeled B16F10 cells, which lack the *BRAF* mutation (Fig. 1D) (Huh et al., 2023). Analysis of GFP-positive and CD45-negative cells from the published dataset (Korea BioData Station accession number: KAP230547) identified 882 primary tumor cells, 883 CTCs, and 1,223 metastatic tumor cells (Fig. 1E), with the majority expressing melanocyte markers (Supplementary Fig. S2A, B). Throughout the metastatic cascade, we observed consistent dynamics in the expression of ECM and hemoglobin genes, indicating AST-associated transcriptional changes (Fig. 1F). To exclude the possibility that hemoglobin transcripts originated from ambient RNA contamination, we performed immunofluorescence staining on GFP-labeled B16F10 CTCs. Hemoglobin A (HbA) protein was detected within the cytoplasm of GFP-positive tumor cells, confirming tumor-intrinsic expression during dissemination (Supplementary Fig. S2C).

To corroborate these findings, we analyzed a bulk RNA-seq dataset from a genetically engineered *Braf*$^{CA/+}$;*Pten*$^{flox/flox}$ mouse model of melanoma (GSE52031; Fig. 1G) (Luo et al., 2014). Paired transcriptomic analysis revealed a marked increase in AST gene expression during CTC generation, followed by a reduction during metastatic colonization, suggesting that AST induction is transient (Fig. 1H). The results from these 3 types of melanoma mouse models demonstrate that AST plasticity during the metastatic process is independent of the tumor's mutational profile.

To assess whether AST-associated transcriptional features are detectable in human melanoma, we analyzed an independent scRNA-seq dataset profiling CTCs and peripheral blood mononuclear cells (GSE157745; Fig. 1I) (Hong et al., 2021). Although the cohort is limited and lacks matched primary-CTC pairs, we observed that a subset of CTCs showed elevated expression of AST genes compared with circulating leukocytes (Fig. 1J). While these findings suggest a trend toward increased AST gene expression in circulating melanoma cells, further studies involving larger, matched sample cohorts are warranted to definitively establish the clinical significance of AST in human melanoma.

To determine whether AST plasticity is unique to melanoma or represents a mechanism applicable to other cancer types, we extended our analysis to an orthotopic model of pancreatic ductal adenocarcinoma, driven by *Kras* G12D mutation and *Trp53* loss (Simeonov et al., 2021). scRNA-seq analysis of paired primary tumors, CTCs, and metastatic lesions from this pancreatic ductal adenocarcinoma model revealed remarkably similar AST gene dynamics to those observed in melanoma: AST genes were upregulated in CTCs and returned to baseline levels in established metastases (Supplementary Fig. S2D-F). Additionally, ECM and hemoglobin gene expression patterns mirrored those seen in melanoma throughout the metastatic process (Supplementary Fig. S2G, H). These results demonstrate that AST represents a conserved transcriptional program that orchestrates hematogenous tumor dissemination across different cancer types, independent of the specific oncogenic drivers.

AST Expression Contributes to Clone Aggressiveness

Immunocytochemical analysis of B16F10-derived CTCs revealed heterogeneous expression of AST genes, with IKZF1 showing variable staining intensity across individual CTCs (Fig. 2A). Given the nonuniform expression of AST genes among CTCs, we hypothesized that activation of the AST program may confer a biological advantage for metastatic seeding. To determine whether the induction of AST genes enhances the metastatic potential of melanoma cells, we performed clonal phylogenetic analysis on the scRNA-seq datasets from both orthotopic melanoma mouse models. This analysis utilized the Numbat algorithm, a computational method for inferring CNVs from transcriptomic data (Fig. 2B) (Gao et al., 2023).

CNV-based stratification of the A375 orthotopic mouse model identified 4 distinct tumor clones (Fig. 2C). The inferred phylogenetic structure revealed a stepwise subclonal evolution: the addition of a deletion in chromosome 22 facilitated the conversion from Clone 1 to Clone 2, while a subsequent deletion in chromosome 6 mediated the transition from Clone 2 to Clone 3. Finally, a deletion in chromosome 14 led to the emergence of Clone 4 from the Clone 3 lineage (Supplementary Fig. S3A). Among them, Clone 1 was disproportionately enriched for metastatic tumor cells relative to primary tumor cells (Fig. 2D and Supplementary Fig. S4A, B). While clone sizes in our scRNA-seq dataset are imbalanced, the use of proportion-based Chi-square testing demonstrates that metastatic success is driven by clonal fitness rather than sheer abundance. Clone 1 is significantly enriched in metastatic sites compared with the rest of the population (63.2% vs 20.4%, $P < .001$; Supplementary Table S1).

Moreover, CTCs within Clone 1 exhibited significantly elevated expression of AST genes relative to CTCs from other clones (Fig. 2E and Supplementary Fig. S4C). To further understand the unique characteristics of Clone 1, we examined its transcriptional signatures. Clone 1-derived CTCs exhibited reduced expression of ECM genes and genes involved in hypoxia and reactive oxygen species (ROS) pathways (Supplementary Figs. S4D and S5). Notably, anoikis signature scores differed across A375 CTC clones (Kruskal-Wallis $P = 1.5 \times 10^{-8}$), with Clone 1 exhibiting significantly lower scores than the other 3 clones in post hoc testing (Bonferroni-adjusted *P*-values in Supplementary Fig. S4E), indicating an enhanced capacity to resist anoikis during circulation.

Subsequent validation using the B16F10 mouse model further supported these findings. Clonal evolution in this model was primarily characterized by successive Copy Number Loss of Heterozygosity (CNLoH) events, beginning with alterations in chromosomes 3 and 7 (Clone B), followed by the acquisition of CNLoH in chromosome 10 (Clone C), and culminating in chromosome 14 CNLoH in the terminal lineage (Supplementary Fig. 3B). Among the 4 identified clones, Clone D exhibited the highest metastatic potential, with the greatest proportion of metastatic tumor cells relative to primary tumor cells (Fig. 2F, G and Supplementary Fig. S4F, G). Although statistical significance was not reached likely due to smaller sample sizes in the other clones, Clone D showed a higher metastatic

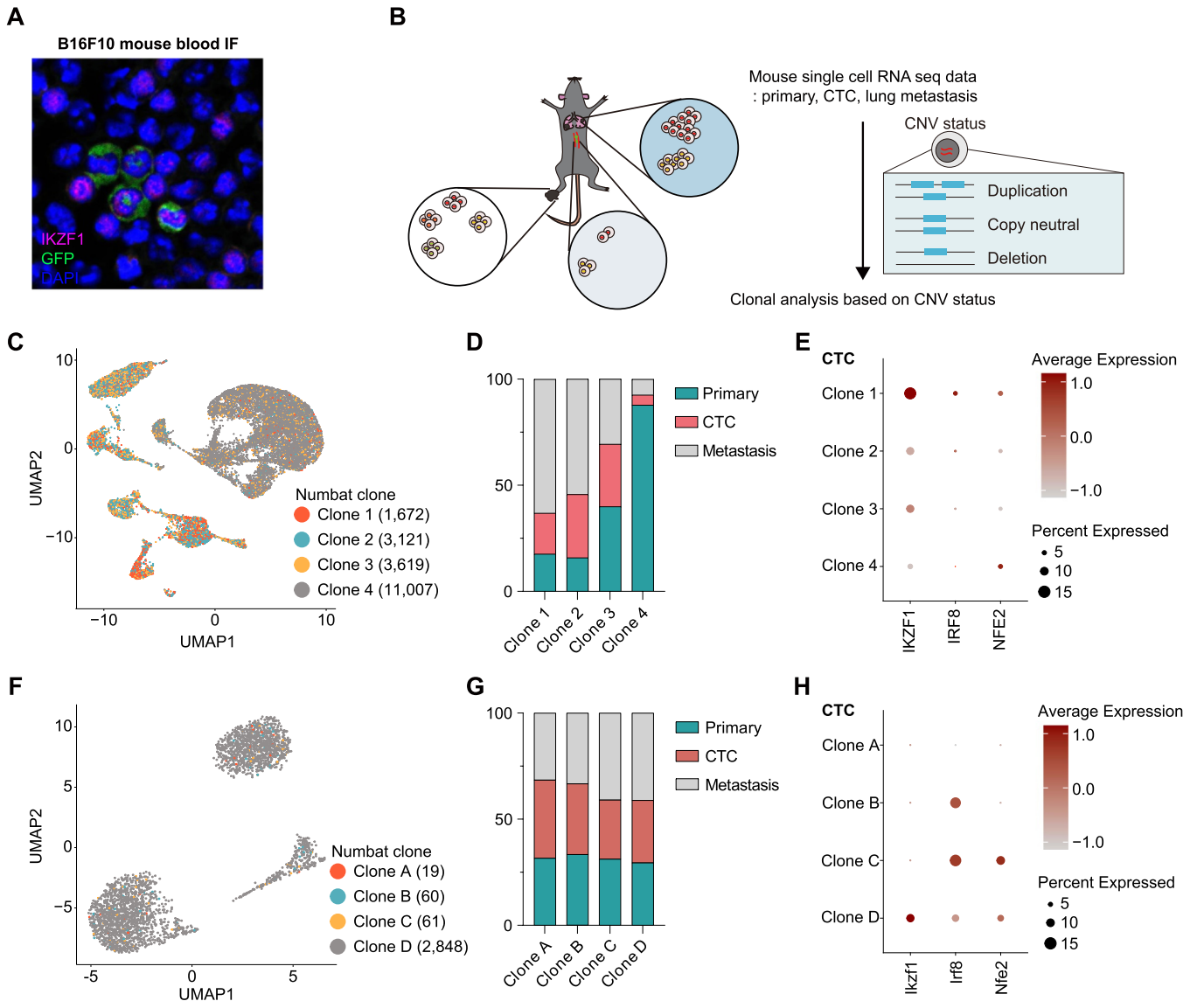

Fig. 2. *Impact of AST expression on the metastatic potential of tumor clones.* (A) Representative immunofluorescence image of a CTC from the GFP-positive B16F10 mouse melanoma model, stained for GFP (tumor, green), IKZF1 (red), and DAPI (nuclei, blue). (B) Schematic representation of clonal analysis workflow using the Numbat package to infer clonal structure from copy number variation (CNV) profiles. (C) UMAP visualization of the clonal phylogenetic structure of A375-derived tumor cells, inferred from single-cell CNV profiles. Cells are color-coded based on their assigned clones: Clone 1 (red, $n = 1,672$), Clone 2 (blue, $n = 3,121$), Clone 3 (yellow, $n = 3,619$), and Clone 4 (dark gray, $n = 11,007$). (D) Proportional distribution of primary tumor cells (blue), CTCs (red), and metastatic tumor cells (gray) across the 4 identified clones. Clone 1 shows the highest proportion of metastatic tumor cells compared with that of primary tumor cells. (E) Dot plot showing the average expression levels of AST genes *IKZF1*, *IRF8*, and *NFE2* in CTCs across the 4 A375-derived clones. AST gene expression is upregulated in clone 1, suggesting a link between AST activation and metastatic capacity. (F) UMAP visualization of the clonal phylogenetic structure of B16F10-derived tumor cells, inferred from single-cell CNV profiles. Clones are color-coded as follows: Clone 1 (red, $n = 19$), Clone 2 (blue, $n = 60$), Clone 3 (yellow, $n = 61$), and Clone 4 (dark gray, $n = 2,848$). (G) Proportional distribution of primary tumor cells (blue), CTCs (red), and metastatic tumor cells (gray) across the 4 identified clones in the B16F10 model. Similar to the A375 model, clone 4 exhibits the highest metastatic potential. (H) Dot plot illustrating the average expression levels of *Ikzf1*, *Irf8*, and *Nfe2* in CTCs across the 4 B16F10-derived clones. AST gene expression is upregulated in clone 4, reinforcing its association with AST induction and metastatic potential. CNV, copy number variation; CTC, circulating tumor cell; IF, immunofluorescence staining.

proportion compared with the aggregate of other clones (41.2% vs 36.4%, $P = .267$; Supplementary Table S2), consistent with the trend observed in the A375 model. Paralleling observations in the A375 model, Clone D-derived CTCs expressed the highest levels of AST genes (Fig. 2H and Supplementary Fig. S4H), and showed a reduction in hypoxia- and ROS-associated signatures (Supplementary Fig. S4I). However, unlike the A375 model, anoikis signature scores did not differ significantly across B16F10 CTC clones (Kruskal-Wallis $P = .462$; Supplementary Fig. S4J), though the overall trend remained

consistent. Collectively, these findings demonstrate that AST-high CTCs are more likely to contribute to successful metastatic colonization, supporting the functional significance of AST in driving melanoma progression.

An AST Continuum Exists Independent of the EMT-Like Transition

Next, we aimed to clarify the relationship between AST- and EMT-like transition during melanoma dissemination by analyzing genes associated with EMT- or MET-like transitions using scRNA-seq datasets from 2 orthotopic melanoma mouse models. We found that the expression of 3 AST genes was upregulated in CTCs, whereas genes associated with EMT-like transition, such as *AXL* and *ZEB1* (Pedri et al., 2022), displayed inconsistent expression patterns (Supplementary Fig. S6A, B). Conversely, the expression of markers typically linked to MET-like transition, including MITF and ZEB2 (Pedri et al., 2022), was upregulated in CTCs (Supplementary Fig. S6A, B). These observations suggested that AST- and EMT-like transition may occur via distinct pathways during the metastatic progression of melanoma. Consistent with this notion, AST-positive cells were significantly depleted among EMT-like transition-positive cells in the A375-derived model ($P < .001$; Supplementary Table 3). A similar trend was observed in the B16F10-derived model, although it did not reach statistical significance ($P = .390$; Supplementary Table 4).

EMT has traditionally been regarded as a binary process, with cells transitioning from a purely epithelial to a fully mesenchymal state (Boyer and Thiery, 1993). However, recent findings have redefined EMT as a spectrum encompassing partial or hybrid states (Hong et al., 2015; Lu et al., 2013; McFaline-Figueroa et al., 2019; Pastushenko and Blanpain, 2019; Williams et al., 2019). Drawing on this conceptual framework, we hypothesized that AST occurs similarly along a continuum. To clarify this intermediate state, we introduced the concept of "AST-priming," which describes adherent primary tumor cells that have begun to acquire AST-related transcriptional features but have not yet undergone physical detachment.

Analysis of primary tumor scRNA-seq data showed that AST-positive cells did not form a discrete transcriptional cluster (Fig. 3A, C and Supplementary Fig. S6C, D), implying that AST induction occurs along a continuum rather than as a binary switch. Monocle 3 trajectory analysis further revealed a progressive increase in AST gene expression along the pseudotime axis, consistent with a graded AST-priming trajectory (Fig. 3B, D) (Cao et al., 2019).

This trajectory originates from fully adherent cells with minimal *IKZF1*, *IRF8*, and *NFE2* expression and progresses toward cells exhibiting strong suspension-associated transcriptional programs. Notably, the 3 AST genes displayed coordinated upregulation along the AST-priming trajectory, whereas EMT-like and MET-like transition markers showed heterogeneous and often uncoordinated expression dynamics (Fig. 3B, D and Supplementary Fig. S6E-H).

To further validate the AST continuum, we performed pseudotime trajectory analyses comparing primary tumor cells and CTCs, enabling us to trace the transition from adherent tumor cells to suspension-like CTCs within our model (Fig. 3E-H). Our results revealed a progressive upregulation of AST gene expression during the transition, whereas genes associated with EMT-like and MET-like transitions exhibited variable and inconsistent expression patterns (Fig. 3F, H). Taken together, these findings indicated that AST emergence within the primary tumor is largely independent of traditional EMT-like or MET-like transitions during melanoma metastasis.

Spatial Transcriptomics Reveal AST-Positive Melanoma Cells in Close Vascular Proximity

Having defined the role of AST in CTC formation, we next investigated where AST-positive cells are spatially positioned within the tumor microenvironment. To achieve this, we conducted spatial transcriptomic profiling of primary tumors from the B16F10 orthotopic melanoma model using the Xenium platform (10x Genomics; Fig. 4A). Unsupervised clustering and cell-type annotation identified 15 distinct clusters, including melanoma cells, immune cells, endothelial cells, and a small population of stem cells (Supplementary Fig. S7A, B). This analysis enabled us to examine the spatial association between AST-positive cells and key tumor microenvironment components, including EMT-like and MET-like transitioned cells and endothelial cells. Histological and transcriptomic analyses of the B16F10 primary tumor revealed that AST-positive tumor cells, marked by *Ikzf1*, *Irf8*, and *Nfe2* expression, were transcriptionally distinct from EMT-like and MET-like transitioned cells (Fig. 4B and Appendix AC). Quantification of AST-positive cell proportions demonstrated their presence across EMT-like transitioned and non–EMT-associated tumor cell populations (Fig. 4C). Intriguingly, we observed a spatial enrichment of AST-positive cells in close proximity to CD31-expressing endothelial cells compared with EMT-positive cells (Fig. 4D). Quantitative assessment of vascular proximity showed that AST-positive cells displayed a significantly shorter distance to the nearest blood vessel compared with that of EMT-positive cells (Wilcoxon $P = 1.3 \times 10^{-10}$; Fig. 4E and Supplementary Fig. S7D).

To evaluate whether the spatial relationship between AST-positive tumor cells and the vasculature was conserved in human disease, we analyzed a publicly available Visium spatial transcriptomics dataset of human melanoma tissue provided by 10x Genomics (Fig. 4F). Based on canonical marker gene expression, we classified cells into 7 major subtypes: AST-positive tumor cells, AST-negative tumor cells, endothelial cells, T-cells, macrophages, fibroblasts, B-cells, and keratinocytes (Supplementary Fig. S8A). Consistent with observations in the murine model, AST-positive tumor cells in the human sample were preferentially located near endothelial cells, indicating a conserved spatial relationship. Spearman correlation analysis revealed a significant negative association between *IKZF1* expression and the distance to the nearest blood vessel ($R = -0.13$, $P = 1.1 \times 10^{-6}$). *IRF8* showed a comparable negative trend, whereas *NFE2* displayed a weaker spatial association (Fig. 4G).

To validate these spatial associations, we conducted immunofluorescence staining of primary mouse melanoma tissue. Analysis of B16F10-derived tumors confirmed that IKZF1-positive melanoma cells were predominantly localized in close proximity to CD31-positive endothelial cells (Fig. 4H),

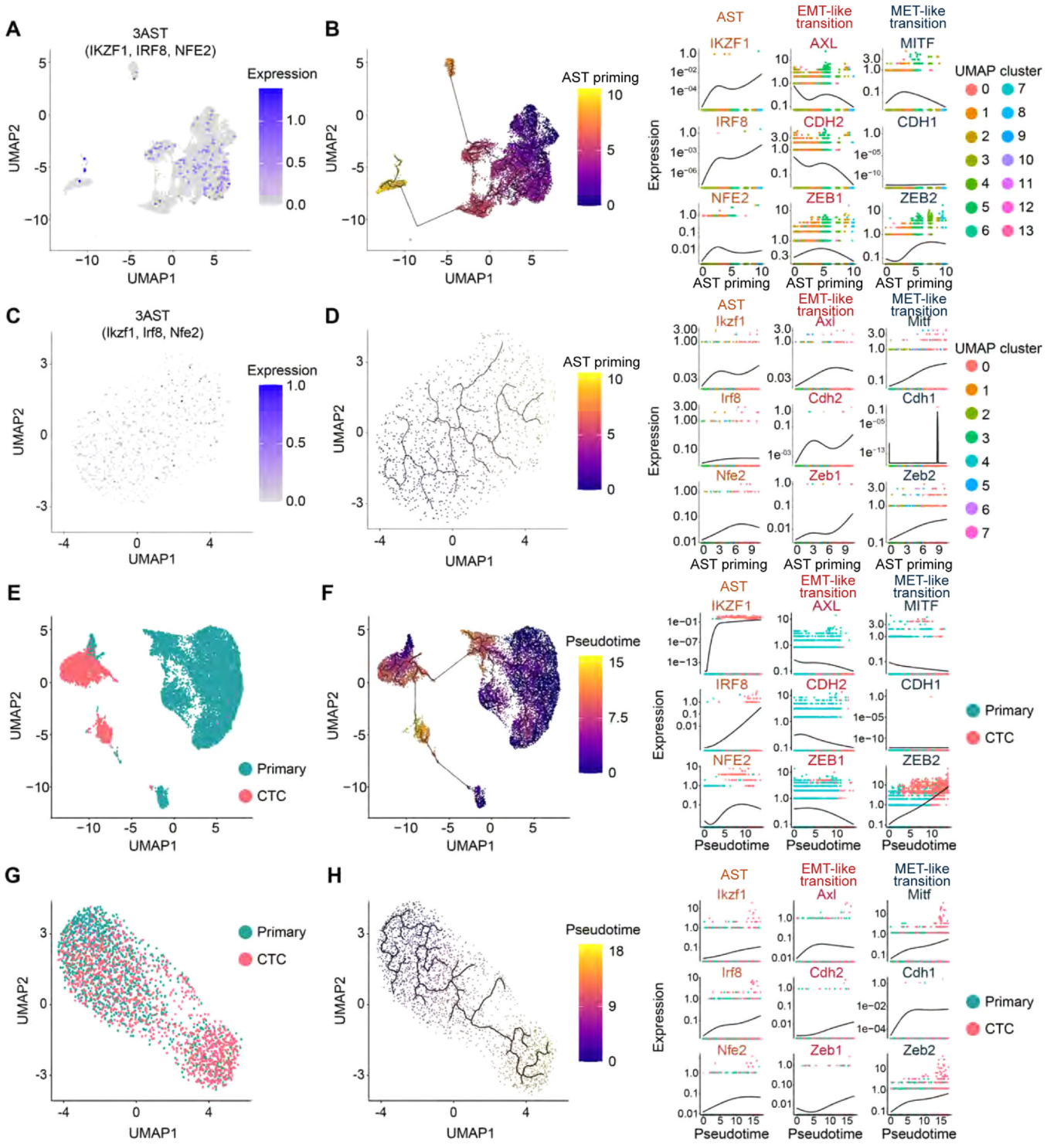

(caption on next page)

Fig. 3. *EMT-like transition during the metastatic cascade and transcriptional AST continuum in vivo.* (A) Feature plot of AST genes (*IKZF1*, *IRF8*, and *NFE2*) in the A375-derived primary tumor cells. (B) Left panel: Monocle-derived trajectory analysis defining the AST-priming continuum in A375-derived primary tumor cells. Cell transition from a baseline adherent state toward a suspension transition-ready state. Right panel: Expression kinetics of selected AST (orange), EMT-like (red; *AXL*, *CDH2*, and *ZEB1*), and MET-like transition-related genes (navy; *MITF*, *CDH1*, and *ZEB2*) along the AST-priming axis, illustrating their distinct transcriptional trends. (C) Feature plot of AST genes, *Ikzf1*, *Irf8*, and *Nfe2*, in the B16F10-derived primary tumor cells. (D) Left panel: Monocle-derived AST-priming trajectory for B16F10-derived primary tumor cells based on UMAP embeddings. Right panel: Expression kinetics of selected AST-, EMT-like, and MET-like transition-related genes along the AST-priming continuum, demonstrating their distinct transcriptional trends. (E) UMAP embedding of the analyzed transcriptomes of 11,899 primary tumor cells (blue) and 2,838 CTCs (red), highlighting transcriptional differences. (F) Left panel: Monocle-derived pseudotime trajectory showing the progression from primary tumor cells to CTCs. Right panel: Pseudotime kinetics of AST-, EMT-like, and MET-like genes along the trajectory, showing the dynamic transcriptional shifts associated with CTC generation. (G) UMAP embedding of 882 B16F10-derived primary tumor cells (blue) and 883 CTCs (red), illustrating distinct cellular populations. (H) Left panel: Monocle-derived pseudotime trajectory demonstrating the transition from primary tumor cells to CTCs in the B16F10 model. Right panel: Pseudotime kinetics of AST-, EMT-like, and MET-like genes, further supporting the presence of an AST continuum independent of EMT-like and MET-like transitions. AST, adherent-to-suspension transition; CTC, circulating tumor cell.

supporting a potential link between AST expression and vascular accessibility. Furthermore, to investigate the molecular mechanism underlying this association, we performed cellular interaction mapping based on the human melanoma Visium dataset (Jin et al., 2023). Circle plot and heatmap analysis demonstrated strong interactions between AST-positive tumor cells and endothelial cells, distinguishing them from AST-negative counterparts (Fig. 4I). Specifically, ligand-receptor interaction analysis identified an interactome between the AST-positive subpopulation and endothelial cells, characterized by enriched signaling probabilities in conserved vascular interaction axes (Supplementary Fig. S8B). These findings suggest that AST-positive melanoma cells may occupy a unique perivascular niche, potentially contributing to their enhanced metastatic potential.

AST Genes Reprogram the Anchorage Dependency of Adherent Cells

Building on these spatial insights, we next sought to mechanistically dissect how AST contributes to anchorage independence and metastatic dissemination using in vitro systems. Melanoma metastasis involves a complex process of cellular reprogramming that enables tumor cells to transit between adherent and suspension states. While conventional metastasis assays typically focus on migration and invasion (Lee et al., 2024a), yet the process of dissemination from the primary tumor remains poorly understood. To bridge this gap, we established an in vitro "dissemination assay" that recapitulates the key steps of detachment, circulation, and reattachment in the metastatic cascade (Fig. 5A). Given that high cell density often leads to competitive displacement of latent metastatic cells (Kim et al., 2023), we hypothesized that a portion of cancer cells might detach from culture plates when subjected to prolonged high-cell-density environments. To explore this, we utilized various melanoma cell lines derived from humans and mice, including A375 and B16F10. We observed that a subset of cells spontaneously detached under prolonged high-density conditions (Supplementary Fig. S9A-C). Annexin V/propidium iodide flow cytometry demonstrated that majority of detached CTC-like cells remained viable (Annexin V^-/PI^-), with minimal proportions of apoptotic or necrotic cells in both B16F10 and A375 (Supplementary Fig. 10A, B). Moreover, when these CTC-like cells were transferred to a new plate, they reattached and proliferated, forming metastasis-like colonies. Together, these results indicate that the transition to a suspended state is a controlled biological event rather than a by-product of cell death or detachment-induced apoptosis.

To determine whether the AST program is required for melanoma cell detachment, we performed loss-of-function experiments using lenalidomide, a clinical-grade immunomodulatory drug that induces IKZF1 degradation. Consistent with our previous finding that CRISPR-/Cas9-mediated *Ikzf1* knockout reduces CTC formation without affecting primary tumor growth in vivo (Huh et al., 2023), pharmacological inhibition of IKZF1 significantly reduced the generation of CTC-like cells in the dissemination assay (Supplementary Fig. S9D). These findings support a functional requirement for AST activity during the transition to an anchorage-independent state.

Quantitative real-time PCR (qPCR) of cells at different assay stages revealed a significant upregulation in the expression of AST genes in CTC-like cells, whereas that of EMT-like and MET-like transition markers exhibited differential trends across primary-like, CTC-like, and metastasis-like states (Fig. 5B and Supplementary Fig. S9A). Notably, while *IKZF1* and *IRF8* showed consistent and statistically significant upregulation across comparisons, *NFE2* expression showed variability across conditions and did not reach statistical significance in all comparisons. These findings suggested that AST regulates tumor cell dissemination independently from classical EMT or MET pathways.

To further characterize AST-mediated transcriptional changes, we recapitulated the AST phenotype in melanoma by engineering a doxycycline-inducible B16F10-3AST^{TetR} cell line in which *IKZF1*, *IRF8*, and *NFE2* can be synchronously activated (Fig. 5C). Upon doxycycline induction, these 3 transcription factors were upregulated, driving melanoma cells into a suspension state associated with reduced anchorage dependence. Importantly, this transition was fully reversible: withdrawal of doxycycline restored the adherent phenotype, demonstrating that AST is a plastic and responsive program in melanoma cells (Fig. 5D). PCA demonstrated clear separation between mock-treated and AST-induced suspended cells (Supplementary Fig. S10A), with Western blot analysis confirming robust upregulation of IKZF1, IRF8, and NFE2 proteins upon AST induction (Supplementary Fig. S10B, C). Transcriptomic analysis of AST-induced suspended cells confirmed

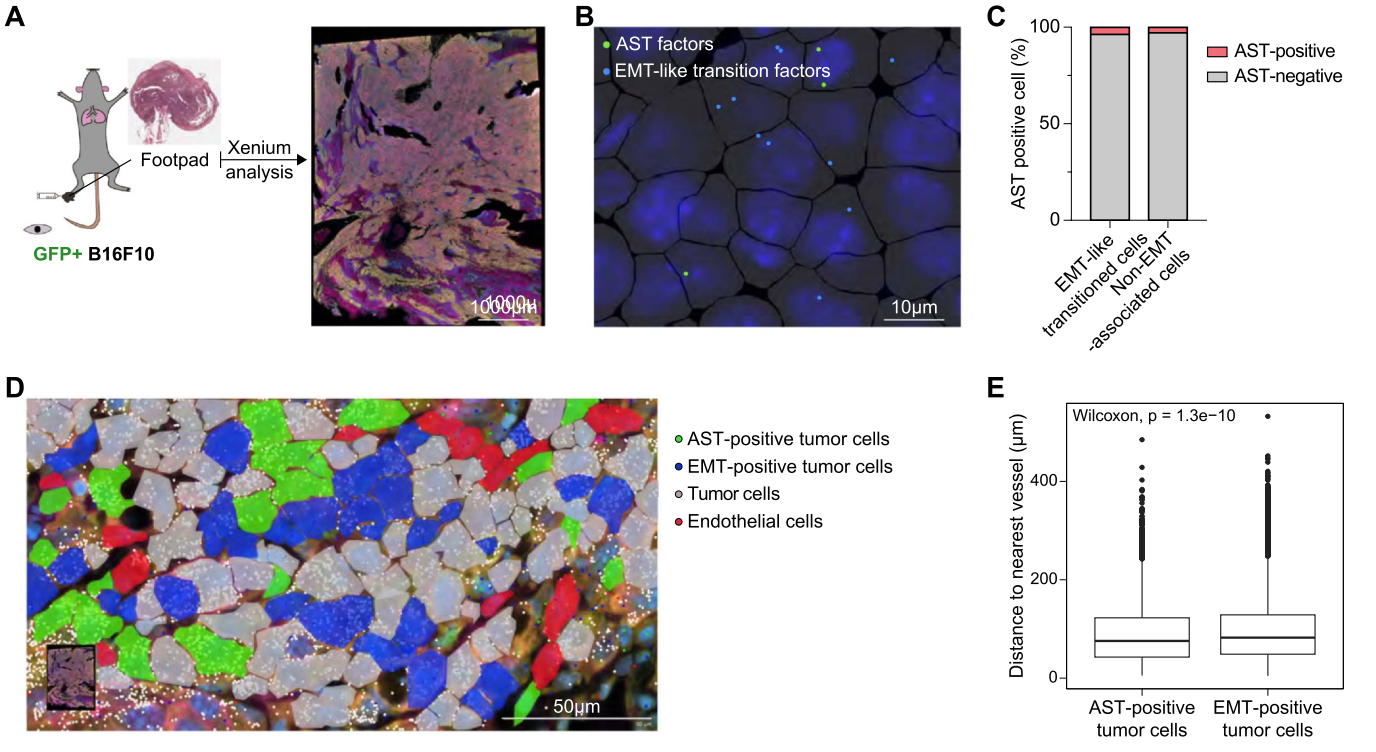

(caption on next page)

Fig. 4. *Spatial transcriptomics reveals AST-positive melanoma cells in close vascular proximity across mouse and human models.* (A) Schematic representation of the study design and spatial transcriptomics analysis. The primary footpad tumor was preserved as a formalin-fixed paraffin-embedded (FFPE) sample and subjected to Xenium spatial transcriptomic analysis. The right panel displays a representative Xenium dataset, providing a spatial overview of gene expression within the tumor microenvironment. (B) Overlaid spatial mapping of gene expression. EMT-like transition genes (*Axl*, *Cdh2*, and *Zeb1*) are marked in blue and AST genes (*Ikzf1*, *Irf8*, and *Nfe2*) in green. AST-positive cells are transcriptionally distinct from EMT-like transitioned cells. (C) Proportion of AST-positive cells across EMT-like transitioned cells and non-EMT-associated cells. Bar plot shows the percentage of AST-positive cells within EMT-like and non-EMT-associated cells in the Xenium dataset. (D) Spatial distribution of AST-positive and EMT-like transitioned cells relative to endothelial cells. AST-positive (green), EMT-positive (blue), endothelial (red), and tumor (gray) cells are mapped within the tumor microenvironment. AST-positive cells are preferentially localized closer to endothelial cells compared with EMT-positive cells. (E) Quantitative analysis of AST-positive cell proximity to blood vessels. Boxplot comparing the distance to the nearest vessel for AST-positive and EMT-like transitioned cells. AST-positive cells exhibit significantly shorter distances to the vasculature (Wilcoxon $P = 1.3 \times 10^{-10}$), supporting their potential role in tumor dissemination via vascular proximity. The boxplot represents the median and interquartile range (IQR), with whiskers extending to 1.5 × IQR. Statistical significance was determined by the Wilcoxon rank-sum test. (F) Spatial transcriptomic analysis of human melanoma illustrating the distribution of AST-positive cells. AST-positive tumor cells (blue), endothelial cells (red), and AST-negative tumor cells (yellow) are mapped within the tumor microenvironment. AST-positive cells are enriched in close proximity to blood vessels, suggesting a potential association between AST expression and vascular accessibility. (G) Correlation between AST gene expression and vascular proximity. Spearman's correlation analysis of *IKZF1*, *IRF8*, and *NFE2* expression with the distance to the nearest blood vessel in the human melanoma Visium dataset. A significant negative correlation is observed for *IKZF1* ($R = -0.13$, $P = 1.1 \times 10^{-6}$), with *IRF8* and *NFE2* also showing a weak trend toward negative correlation. (H) Immunofluorescence staining of B16F10-derived primary tumors. Blue, DAPI; green, GFP (melanoma); red, CD31; pink, IKZF1. IKZF1-positive melanoma cells are located in close proximity to CD31-positive endothelial cells, indicating a spatial association between AST-positive melanoma cells and the vasculature. (I) Cellular interaction analysis in the tumor microenvironment. Left: Circle plot depicting the interaction strength between tumor cells and various cell types, including endothelial cells, fibroblasts, macrophages, T-cells, B-cells, and keratinocytes, based on the human melanoma Visium dataset. Right: Heatmap quantifying interaction strengths between AST-positive and AST-negative tumor cells and stromal/immune components. AST-positive tumor cells exhibit strong interactions with endothelial cells, highlighting a unique microenvironmental niche potentially contributing to their metastatic capacity. AST, adherent-to-suspension transition; EMT, epithelial-to-mesenchymal transition; MET, mesenchymal-to-epithelial transition.

the significant upregulation in the expression of AST genes, alongside the downregulation in the expression of the Hippo signaling pathway, consistent with previous observations (Fig. 5E). In addition, we noted that AST-induced cells exhibited reduced adhesion, attributed to a decline in cell-matrix interactions rather than alterations in cell-cell adhesion, further supporting the role of AST in reprogramming anchorage dependence (Huh et al., 2023).

To assess whether AST induction influences EMT-like or MET-like transcriptional states, we compared the gene expression profiles of mock versus AST-induced suspended cells. Single-sample GSEA revealed that the expression of EMT-related pathways was downregulated in AST-induced cells, further distinguishing AST from EMT-like transitions in melanoma metastasis. The expression of EMT-like transition genes was predominantly upregulated in control cells, whereas MET-like transition genes were upregulated in AST-induced cells (Fig. 5F). Nonetheless, we observed inconsistent patterns among these genes, resulting in nonsignificant GSEA (Supplementary Fig. S9D). Thus, our observations indicated that AST reprograms anchorage dependence independently of EMT-like or MET-like transition pathways.

DISCUSSION

The prevailing view on metastasis is primarily focused on genetic alterations. However, the recent discovery of common mutations between primary and metastatic tumors indicates the role of additional nongenetic elements (Heo et al., 2023; Lin et al., 2022; Reiter et al., 2019; Reiter et al., 2018). This shift has sparked interest in cellular plasticity and the impact of environmental factors on cell traits, such as morphology and anchorage dependence during metastasis. In this study, we identified the induction of AST genes as a key driver of cellular plasticity during melanoma dissemination. While previous studies established a 4-gene AST signature (*IKZF1*, *IRF8*, *NFE2*, and *BTG2*) (Huh et al., 2023; Lee et al., 2024a), our analysis of paired primary-CTC-metastasis samples revealed that *BTG2* exhibited elevated expression in metastatic lesions rather than CTCs, displaying distinct kinetics from the other AST genes. Based on this differential expression pattern, we engineered a doxycycline-inducible B16F10-3AST^{TetR} melanoma cell line to test whether *IKZF1*, *IRF8*, and *NFE2* were sufficient to drive AST. Doxycycline induction triggered rapid loss of adhesion and suspension growth, whereas doxycycline withdrawal restored adherence, demonstrating a reversible, 3-factor-driven AST in melanoma. Using orthotopic mouse models of melanoma, we demonstrated that CTCs undergo transient upregulation of AST genes—*IKZF1*, *IRF8*, and *NFE2*—distinctly separating them from both primary and metastatic tumor cells. The induction of AST was accompanied by downregulation of ECM genes and upregulation of hemoglobin genes, suggesting that AST facilitates cellular detachment and intravasation. Insights into AST plasticity may pave the way for new therapeutic approaches targeting the metastatic spread of cancer.

Our findings were consistent across multiple in vivo models of melanoma. We examined 3 distinct systems: human A375 melanoma cells (harboring a *BRAF* mutation) in immunodeficient NOG mice, murine B16F10 cells (lacking *Braf* mutations) in immunocompetent C57BL/6 mice, and a genetically engineered mouse model driven by constitutively active *Braf* mutation and *Pten* loss. Despite differences in species origin, mutational profiles, and immune contexts, AST gene expression was consistently elevated in CTCs across all 3 models. This conservation

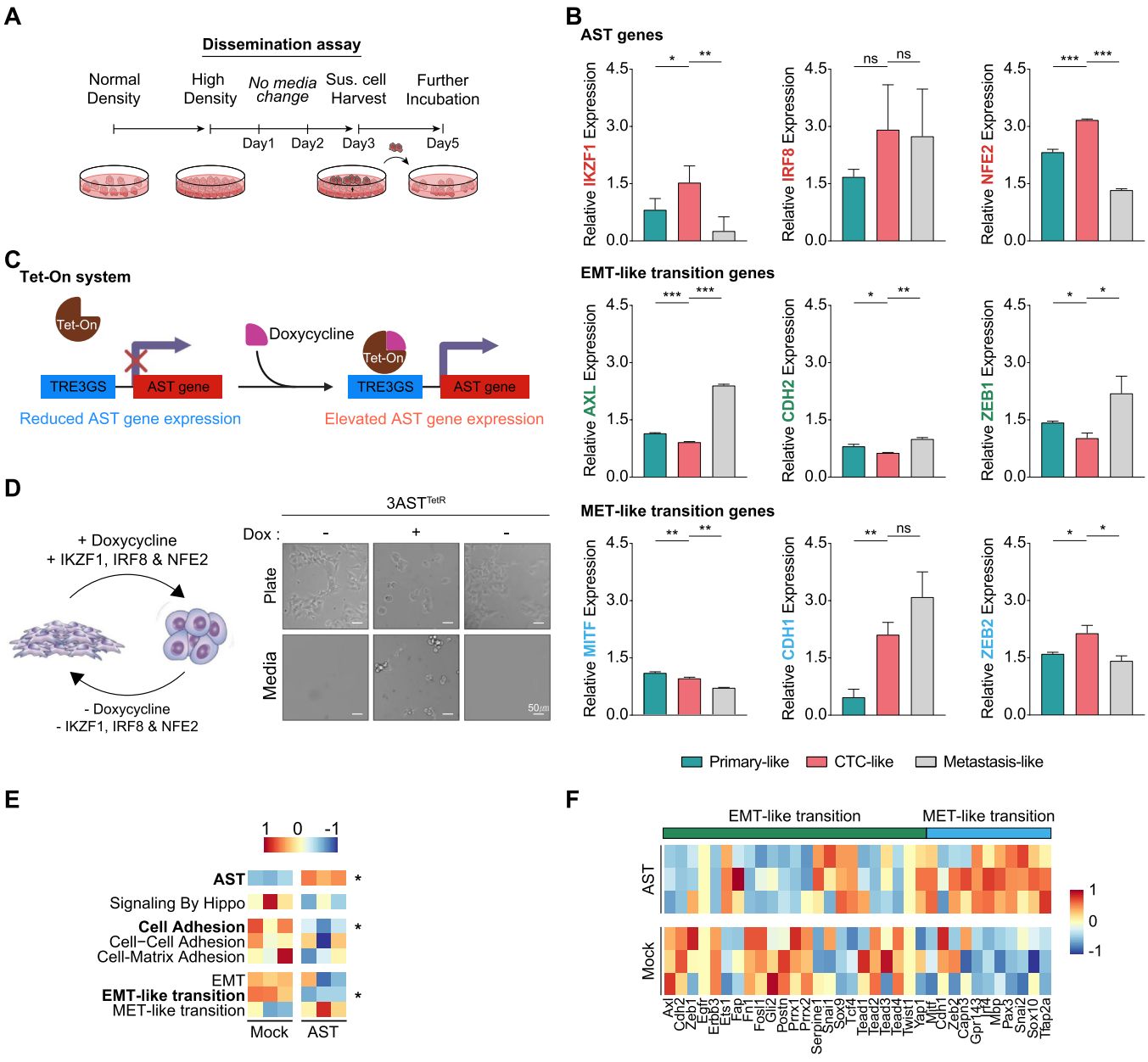

Fig. 5. *In vitro dissemination assay recapitulates transient AST induction during the metastatic cascade.* (A) Schematic overview of the in vitro dissemination assay. Primary-like, CTC-like, and metastasis-like cells were harvested for further analysis. (B) Relative expression of AST-, EMT-like, and MET-like transition genes throughout the dissemination assay. Gene expression levels were assessed across 3 cellular states: primary-like, CTC-like, and metastasis-like cells. The expression of AST genes (*IKZF1*, *IRF8*, and *NFE2*) was significantly upregulated in CTC-like cells, whereas EMT-like (*AXL*, *CDH2*, and *ZEB1*) and MET-like (*MITF*, *CDH1*, and *ZEB2*) transition markers displayed differential expression patterns, supporting an independent AST trajectory. Data are presented as mean ± SD. *P* values determined by 2-tailed unpaired Student's *t*-test. **P* < .05, ***P* < .01, ****P* < .001. (C) Schematic overview of the doxycycline-inducible system for engineering B16F10-3AST^{TetR} cells, enabling controllable induction of AST genes for repeated detachment-reattachment experiments. (D) Conceptual workflow illustrating reversible AST induction: doxycycline induces *IKZF1*, *IRF8*, and *NFE2*, promoting AST; withdrawal restores adherent phenotype, demonstrating AST plasticity in B16F10 cells (left). Dynamic regulation of anchorage dependence in B16F10-3AST^{TetR} cells. Phase-contrast images showing consecutive reprogramming of anchorage dependency following the induction and withdrawal of doxycycline (right). Scale bars, 50 μm. (E) Single-sample gene set enrichment analysis results of AST-induced suspended cells. *P* values determined by 2-tailed unpaired Student's t-test. **P* < .05. (F) Heatmap of EMT-like and MET-like transition gene expression in mock- and AST-induced suspended cells. AST, adherent-to-suspension transition; CTC, circulating tumor cell; EMT, epithelial-to-mesenchymal transition; MET, mesenchymal-to-epithelial transition.

of AST induction—observed in both immunocompromised and immunocompetent settings—suggests that AST represents a fundamental mechanism of melanoma dissemination that operates independently of specific oncogenic drivers or immune system interactions.

Clonal phylogenetic analysis of our scRNA-seq data further supported the functional significance of AST. Clones exhibiting high AST expression in CTCs were enriched for metastatic tumor cells, supporting a functional link between AST and metastatic potential. These AST-high CTCs displayed transcriptional signatures characterized by downregulation of ECM genes and suppression of pathways associated with hypoxia and ROS, suggesting an adaptive advantage for survival in circulation. These findings support the dual role of AST in facilitating both cellular detachment and the selection of aggressive tumor subpopulations with enhanced dissemination potential. By linking AST expression to clonal evolution, our study provides insights into how AST promotes metastasis by expanding highly metastatic clones and highlights the potential for therapeutic interventions targeting AST factors to mitigate cancer metastasis. Notably, while clonal enrichment of AST-high CTCs reached statistical significance in the A375 model, the same trend in the B16F10 model did not. This discrepancy likely reflects the combined effect of B16F10's intrinsically high and relatively uniform metastatic capacity, which may reduce the selective advantage conferred by AST, and the substantially smaller cell numbers recovered in the B16F10 model (2,988 vs 19,419 cells), limiting statistical power. Differences in immune context between the immunodeficient (NOG) host used for A375 and the syngeneic immunocompetent B16F10 system may also independently influence clonal dynamics. Nevertheless, the directionality of enrichment was consistent between models, with Clone D showing the highest metastatic proportion in B16F10 (41.2% vs 36.4%), paralleling Clone 1 enrichment in A375, suggesting that the underlying biology is conserved.

Through trajectory inference analysis, we demonstrated that AST operates independently of EMT-like transition during CTC formation. While melanoma is not of epithelial origin, it undergoes similar plasticity to that observed in epithelial tumors (Pedri et al., 2022). This plasticity, often described as phenotype switching, enables melanoma cells to dynamically reprogram their cellular states, leading to the loss of melanocytic markers, increased invasiveness, and therapy resistance. To further characterize AST dynamics during tumor dissemination and to capture the gradual nature of AST, we introduced the concept of "AST-priming," which describes the progressive transition of primary tumor cells from an adherent to a suspension transition-ready state. Our trajectory inference analysis revealed that AST does not occur as a discrete, binary event but instead progresses along a continuum within the primary tumor. In contrast, EMT-like and MET-like markers exhibited variable and inconsistent expression patterns along the AST-priming trajectory, reinforcing the notion that AST represents a distinct reprogramming event independent of EMT-like or MET-like transitions. This finding challenges the conventional paradigm of metastasis by suggesting that cellular reprogramming during dissemination is not exclusively dependent on EMT but can occur via alternative pathways such as AST. It is important to acknowledge the inherent technical limitations of scRNA-seq data, particularly dropout events in which low-abundance transcripts may not be detected. Accordingly, the observed low expression of EMT-like transition-associated genes in AST-positive cells could partly reflect technical sparsity rather than a complete biological absence. Thus, while our multi-omic and functional data support AST as a reprogramming axis that is largely separable from overt EMT-like transition, we cannot exclude low-level EMT-related activity that may be missed by single-cell sampling depth. A further technical limitation of our scRNA-seq analyses is the use of pooled samples across multiple animals, which was necessary to achieve sufficient CTC capture but precludes pseudobulk or replicate-aware statistical analysis. Accordingly, differential expression statistics derived from these pooled data should be interpreted with appropriate caution, as cell-level comparisons may overestimate statistical significance due to inflated degrees of freedom. Future studies employing sample multiplexing strategies, such as cell hashing or genetic barcoding prior to pooling, would enable per-animal deconvolution and would strengthen the statistical rigor of CTC-focused transcriptomic studies.

Our results also revealed a consistent spatial association of AST-positive cells for vascular proximity in both mouse and human melanoma samples analyzed. However, this observation does not establish a causal relationship. Moreover, the strength of this spatial association varied among AST genes: *IKZF1* and *IRF8* showed consistent perivascular enrichment, whereas *NFE2* displayed a weaker association. It remains unclear whether the perivascular niche actively induces the AST program through angiocrine or physical cues, or whether tumor cells already undergoing AST preferentially migrate toward or accumulate near vascular structures due to altered adhesive or migratory properties. Our spatial data capture this association at a single time point and cannot distinguish between these possibilities. Future studies employing dynamic coculture systems, angiocrine perturbation, or lineage-tracing approaches will be required to resolve the directionality of this relationship. Furthermore, the triggers of AST induction within the primary tumor remain undetermined. These areas would be excellent subjects for future investigation, and employing lineage tracing and single-cell-level spatial transcriptomics may provide insights into the timing and location of AST induction. Moreover, the increased interaction between AST-induced tumor cells and T-cells could be attributed to the immune infiltration driven by upregulated *IKZF1* expression (Chen et al., 2018). Hence, increased immune infiltration and surveillance could serve as potential treatment options, guiding targeted therapies to inhibit AST-driven metastasis.

Another emerging area of interest is the role of AST in facilitating CTC clustering. Prior studies have shown that CTC clusters possess significantly higher metastatic potential than individual CTCs (Aceto et al., 2014; Ring et al., 2023; Szczerba et al., 2019). In our study, AST induction led to reduced cell-ECM adhesion while retaining cell-cell interactions. This selective detachment mechanism may promote the formation of CTC clusters—a hypothesis warranting further investigation through in vivo imaging and cluster-tracing models, given that current single-cell techniques have limitations in capturing CTC clusters.

To decipher the underlying mechanisms of anchorage independence mediated by AST, we established an in vitro dissemination assay that recapitulates the spontaneous detachment, circulation, and reattachment events observed in vivo. In contrast to conventional suspension assays, which rely on trypsinization and fail to mimic the natural process of CTC formation, our assay leverages intrinsic cell competition within high-density cultures to simulate the tumor microenvironment where less fit cells are selectively displaced. Within this system, a distinct subpopulation of melanoma cells spontaneously detached under competitive stress and later reattached to form metastasis-like colonies. These CTC-like cells demonstrated robust upregulation of AST genes while displaying a heterogeneous and diminished expression of EMT-like transition markers. Furthermore, using a doxycycline-inducible system, we demonstrated that AST induction triggers a reversible transition from an adherent to a suspension-like state, highlighting the dynamic plasticity of tumor cells during dissemination. The transcriptomic analysis confirmed that AST-mediated anchorage independence is associated with the downregulation of YAP/TEAD signaling, implicating the suppression of cell-matrix adhesion in AST-driven dissemination. Beyond Hippo signaling, AST involves dynamic integrin remodeling rather than global adhesion loss. While downregulation of ITGAV and related focal adhesion integrins likely facilitates detachment from the primary tumor, the relative enrichment of β1-family integrins in CTCs suggests an adaptive adhesion reprogramming suited to the circulatory environment. This integrin switching may support transient adhesive interactions or cellular aggregation states that enhance survival during dissemination. In addition, the diminished expression of EMT-related pathways in AST-induced cells substantiates that AST occurs independently of EMT-like transition. Taken together, these findings validate our dissemination assay as a physiologically relevant model for studying CTC formation and provide a platform for identifying novel molecular targets for antimetastatic therapies. Future studies employing competitive suspension culture assays, such as coculturing fluorescently labeled AST-high and AST-low populations under nonadherent conditions, could provide direct functional evidence for AST-mediated anoikis resistance and clonal fitness.

The identification of AST genes provides a potential roadmap for therapeutic intervention. We previously demonstrated that clinical-grade IMiDs, such as lenalidomide and pomalidomide, effectively degrade IKZF1 and suppress metastatic seeding in vivo, establishing AST as a druggable vulnerability (Huh et al., 2023). Beyond direct targeting of transcriptional regulators, downstream pathways identified in this study, including YAP/TEAD signaling axis and hemoglobin-mediated redox adaptation, may offer additional opportunities for combination strategies aimed at disrupting the survival advantages of CTCs. Importantly, AST signatures may also serve as biomarkers to identify patients at elevated risk of dissemination and to guide future therapeutic approaches targeting metastasis-specific cellular states.

In summary, this study elucidates the complex mechanism of metastasis involving the AST plasticity in melanoma, which is independent of the EMT-like and MET-like transition pathways. This study highlights the dynamic nature of AST gene expression during metastatic cascades. Ultimately, insights into AST plasticity may lead to novel therapeutic strategies aimed at curbing the metastatic spread of cancer, emphasizing the importance of further exploring this pathway.

FUNDING AND SUPPORT

This work was supported by grants from the National Research Foundation of Korea (RS-2025-00556619, RS-2026-25525017, and RS-2025-18362970 to H.W.P., RS-2025-02214844 to H.Y.G.), the MD-PhD/Medical Scientist Training Program (to D.K.L. and J.O.), the Korean Health Technology R&D Project (RS-2026-25518280 to D.K.L., RS-2025-02223343 to J.O., and RS-2025-25459146 to D.K.L., J.O., H.W.P., and H.Y.G.) through the Korea Health Industry Development Institute (KHIDI), funded by the Ministry of Health & Welfare, Republic of Korea, Korea Basic Science Institute(National research Facilities and Equipment Center) grant funded by the Ministry of Education (RS-2025-02402969 to H.W.P), faculty research grant of Yonsei University College of Medicine (6-2025-0075 to J.O.), and the Yonsei-SCL research grant of Yonsei University College of Medicine (6-2024-0145 to H.Y.G.).

CREDIT AUTHORSHIP CONTRIBUTION STATEMENT

Dong Ki Lee: Writing - review and editing, writing - original draft, visualization, investigation, formal analysis, and data curation. **Jongwook Oh:** Writing - review and editing, writing - original draft, visualization, investigation, formal analysis, and data curation. **Soyeon Lee:** Visualization, investigation, and data curation. **Hyunbin D. Huh:** Investigation. **Yujin Sub:** Investigation. **Kuhn Yoon:** Investigation. **Woo Chul Shin:** Investigation. **Sojin Kim:** Investigation. **Hyun Woo Park:** Writing - review and editing, writing - original draft, supervision, resources, and funding acquisition. **Heon Yung Gee:** Writing - review and editing, writing - original draft, supervision, resources, funding acquisition, and conceptualization.

DECLARATION OF COMPETING INTERESTS

The authors declare that they have no known competing financial interests or personal relationships that could have appeared to influence the work reported in this paper. The author Heon Yung Gee is an Associate Editor for Molecules and Cells and was not involved in the editorial review or the decision to publish this article.

DATA AVAILABILITY STATEMENT

Single-cell RNA-seq data were deposited in the Korean BioData Station (K-BDS, http://kbds.re.kr) under the accession number KAP240742. In this study, we analyzed previously published RNA-seq data deposited at the K-BDS under the accession number KAP230547 and data deposited at the NCBI Gene Expression Omnibus under accession numbers GSE157745, GSE173958, and GSE52031. Spatial transcriptomics data of human melanoma tissues were generated using the Spatial Gene Expression Dataset by SpaceRanger v2.0.0, 10x Genomics (July 13, 2022). Further inquiries can be directed to the corresponding authors.

ACKNOWLEDGMENTS

The authors thank all members of the Gee and Park laboratories for their comments on the paper and their helpful discussions. The authors thank the Yonsei Advanced Imaging Center and Department of Laboratory Animal Resources for technical assistance.

ORCID

Dong Ki Lee https://orcid.org/0000-0002-2830-7640
Kuhn Yoon https://orcid.org/0009-0004-8784-0340
Yung Shin Gee https://orcid.org/0000-0002-8741-6177

APPENDIX A. SUPPORTING INFORMATION

Supplementary data associated with this article can be found in the online version at doi:10.1016/j.mocell.2026.100368.

Received November 24, 2025
Revised April 26, 2026
Accepted April 29, 2026
Available online 12 May 2026.

REFERENCES

Aceto, N., Bardia, A., Miyamoto, D.T., Donaldson, M.C., Wittner, B.S., Spencer, J.A., Yu, M., Pely, A., Engstrom, A., Zhu, H., et al. (2014). Circulating tumor cell clusters are oligoclonal precursors of breast cancer metastasis. Cell, *158*, 1110-1122.

Bakir, B., Chiarella, A.M., Pitarresi, J.R., and Rustgi, A.K. (2020). EMT, MET, plasticity, and tumor metastasis. Trends Cell. Biol. *30*, 764-776.

Bong, D., Sohn, J., and Lee, S.-J.V. (2024). Brief guide to RT-qPCR. Mol. Cells, *47*, Article 100141.

Boyer, B., and Thiery, J.P. (1993). Epithelium-mesenchyme interconversion as example of epithelial plasticity. Apmis, *101*, 257-268.

Cao, J., Spielmann, M., Qiu, X., Huang, X., Ibrahim, D.M., Hill, A.J., Zhang, F., Mundlos, S., Christiansen, L., Steemers, F.J., et al. (2019). The single-cell transcriptional landscape of mammalian organogenesis. Nature, *566*, 496-502.

Chen, J.C., Perez-Lorenzo, R., Saenger, Y.M., Drake, C.G., and Christiano, A.M. (2018). IKZF1 enhances immune infiltrate recruitment in solid tumors and susceptibility to immunotherapy. Cell. Syst. *7*, 92-103.e104.

Gao, T., Soldatov, R., Sarkar, H., Kurkiewicz, A., Biederstedt, E., Loh, P.R., and Kharchenko, P.V. (2023). Haplotype-aware analysis of somatic copy number variations from single-cell transcriptomes. Nat. Biotechnol. *41*, 417-426.

Gerstberger, S., Jiang, Q., and Ganesh, K. (2023). Metastasis. Cell, *186*, 1564-1579.

Heo, H., Kim, H.J., Haam, K., Sohn, H.A., Shin, Y.J., Go, H., Jung, H.J., Kim, J.H., Lee, S.I., Song, K.S., et al. (2023). Epigenetic activation of tensin 4 promotes gastric cancer progression. Mol. Cells, *46*, 298-308.

Hong, T., Watanabe, K., Ta, C.H., Villarreal-Ponce, A., Nie, Q., and Dai, X. (2015). An Ovol2-Zeb1 mutual inhibitory circuit governs bidirectional and multi-step transition between epithelial and mesenchymal states. PLoS Comput. Biol. *11*, Article e1004569.

Hong, X., Roh, W., Sullivan, R.J., Wong, K.H.K., Wittner, B.S., Guo, H., Dubash, T.D., Sade-Feldman, M., Wesley, B., Horwitz, E., et al. (2021). The lipogenic regulator SREBP2 induces transferrin in circulating melanoma cells and suppresses ferroptosis. Cancer Discov. *11*, 678-695.

Huh H.D., Sub Y., Kim J.H., Lee H., Oh J., Lee D.K., Byun J.H., Pyun W.Y., Bae S.J., Pak S., Adherent-suspension plasticity promotes the dissemination and colonization of circulating tumor cells. 2024; bioRxiv. 2024.

Huh, H.D., Sub, Y., Oh, J., Kim, Y.E., Lee, J.Y., Kim, H.R., Lee, S., Lee, H., Pak, S., Amos, S.E., et al. (2023). Reprogramming anchorage dependency by adherent-to-suspension transition promotes metastatic dissemination. Mol. Cancer, *22*, 63.

Jin S., Plikus M.V., Nie Q. CellChat for systematic analysis of cell-cell communication from single-cell and spatially resolved transcriptomics. 2023; bioRxiv. 2023.

Karras, P., Bordeu, I., Pozniak, J., Nowosad, A., Pazzi, C., Van Raemdonck, N., Landeloos, E., Van Herck, Y., Pedri, D., Bervoets, G., et al. (2022). A cellular hierarchy in melanoma uncouples growth and metastasis. Nature, *610*, 190-198.

Kim, G.D., Lim, C., and Park, J. (2024). A practical handbook on single-cell RNA sequencing data quality control and downstream analysis. Mol. Cells, *47*, Article 100103.

Kim, K., Huang, H., Parida, P.K., He, L., Marquez-Palencia, M., Reese, T.C., Kapur, P., Brugarolas, J., Brekken, R.A., and Malladi, S. (2023). Cell competition shapes metastatic latency and relapse. Cancer Discov. *13*, 85-97.

Lee, D.K., Oh, J., Park, H.W., and Gee, H.Y. (2024a). Anchorage dependence and cancer metastasis. J. Korean Med. Sci. *39*, Article e156.

Lee, G.-Y., Ham, S., and Lee, S.-J.V. (2024b). Brief guide to RNA sequencing analysis for nonexperts in bioinformatics. Mol. Cells, *47*, Article 100060.

Lin, D., Shen, L., Luo, M., Zhang, K., Li, J., Yang, Q., Zhu, F., Zhou, D., Zheng, S., Chen, Y., et al. (2021). Circulating tumor cells: biology and clinical significance. Signal Transduct. Target Ther. *6*, 404.

Lin, H., Hu, P., Zhang, H., Deng, Y., Yang, Z., and Zhang, L. (2022). GATA2-Mediated transcriptional activation of Notch3 promotes pancreatic cancer liver metastasis. Mol. Cells, *45*, 329-342.

Love, M.I., Huber, W., and Anders, S. (2014). Moderated estimation of fold change and dispersion for RNA-seq data with DESeq2. Genome Biol. *15*, 550.

Lu, M., Jolly, M.K., Levine, H., Onuchic, J.N., and Ben-Jacob, E. (2013). MicroRNA-based regulation of epithelial-hybrid-mesenchymal fate determination. Proc. Natl. Acad. Sci. U. S. A. *110*, 18144-18149.

Luo, X., Mitra, D., Sullivan, R.J., Wittner, B.S., Kimura, A.M., Pan, S., Hoang, M.P., Brannigan, B.W., Lawrence, D.P., Flaherty, K.T., et al. (2014). Isolation and molecular characterization of circulating melanoma cells. Cell Rep. *7*, 645-653.

Massagué, J., and Ganesh, K. (2021). Metastasis-initiating cells and ecosystems. Cancer Discov. *11*, 971-994.

McFaline-Figueroa, J.L., Hill, A.J., Qiu, X., Jackson, D., Shendure, J., and Trapnell, C. (2019). A pooled single-cell genetic screen identifies regulatory checkpoints in the continuum of the epithelial-to-mesenchymal transition. Nat. Genet. *51*, 1389-1398.

Müller, J., Krijgsman, O., Tsoi, J., Robert, L., Hugo, W., Song, C., Kong, X., Possik, P.A., Cornelissen-Steijger, P.D., Geukes Foppen, M.H., et al. (2014). Low MITF/AXL ratio predicts early resistance to multiple targeted drugs in melanoma. Nat. Commun. *5*, 5712.

Nagrath, S., Sequist, L.V., Maheswaran, S., Bell, D.W., Irimia, D., Ulkus, L., Smith, M.R., Kwak, E.L., Digumarthy, S., Muzikansky, A., et al. (2007). Isolation of rare circulating tumour cells in cancer patients by microchip technology. Nature, *450*, 1235-1239.

Nieto, M.A., Huang, R.Y., Jackson, R.A., and Thiery, J.P. (2016). EMT: 2016. Cell, *166*, 21-45.

Park, G., Kim, S.S., Shim, J., and Lee, S.-J.V. (2025). Brief guide to immunostaining. Mol. Cells, *48*, Article 100157.

Pastushenko, I., and Blanpain, C. (2019). EMT transition states during tumor progression and metastasis. Trends Cell. Biol. *29*, 212-226.

Pedri, D., Karras, P., Landeloos, E., Marine, J.C., and Rambow, F. (2022). Epithelial-to-mesenchymal-like transition events in melanoma. Febs. J. *289*, 1352-1368.

Qiu, X., Mao, Q., Tang, Y., Wang, L., Chawla, R., Pliner, H.A., and Trapnell, C. (2017). Reversed graph embedding resolves complex single-cell trajectories. Nat. Methods, *14*, 979-982.

Reiter, J.G., Baretti, M., Gerold, J.M., Makohon-Moore, A.P., Daud, A., Iacobuzio-Donahue, C.A., Azad, N.S., Kinzler, K.W., Nowak, M.A., and Vogelstein, B. (2019). An analysis of genetic heterogeneity in untreated cancers. Nat. Rev. Cancer, *19*, 639-650.

Reiter, J.G., Makohon-Moore, A.P., Gerold, J.M., Heyde, A., Attiyeh, M.A., Kohutek, Z.A., Tokheim, C.J., Brown, A., DeBlasio, R.M., Niyazov, J., et al. (2018). Minimal functional driver gene heterogeneity among untreated metastases. Science, *361*, 1033-1037.

Ring, A., Nguyen-Sträuli, B.D., Wicki, A., and Aceto, N. (2023). Biology, vulnerabilities and clinical applications of circulating tumour cells. Nat. Rev. Cancer, *23*, 95-111.

Saginala, K., Barsouk, A., Aluru, J.S., Rawla, P., and Barsouk, A. (2021). Epidemiology of melanoma. Med. Sci. (Basel), *9*, 63.

Siegel, R.L., Giaquinto, A.N., and Jemal, A. (2024). Cancer statistics, 2024. CA Cancer J. Clin. *74*, 12-49.

Simeonov, K.P., Byrns, C.N., Clark, M.L., Norgard, R.J., Martin, B., Stanger, B.Z., Shendure, J., McKenna, A., and Lengner, C.J. (2021). Single-cell lineage tracing of metastatic cancer reveals selection of hybrid EMT states. Cancer Cell. *39*, 1150-1162.e1159.

Subramanian, A., Tamayo, P., Mootha, V.K., Mukherjee, S., Ebert, B.L., Gillette, M.A., Paulovich, A., Pomeroy, S.L., Golub, T.R., Lander, E.S., et al. (2005). Gene set enrichment analysis: a knowledge-based approach for interpreting genome-wide expression profiles. Proc. Natl. Acad. Sci. U. S .A. *102*, 15545-15550.

Szczerba, B.M., Castro-Giner, F., Vetter, M., Krol, I., Gkountela, S., Landin, J., Scheidmann, M.C., Donato, C., Scherrer, R., Singer, J., et al. (2019). Neutrophils escort circulating tumour cells to enable cell cycle progression. Nature, *566*, 553-557.

Trapnell, C., Cacchiarelli, D., Grimsby, J., Pokharel, P., Li, S., Morse, M., Lennon, N.J., Livak, K.J., Mikkelsen, T.S., and Rinn, J.L. (2014). The dynamics and regulators of cell fate decisions are revealed by pseudotemporal ordering of single cells. Nat. Biotechnol. *32*, 381-386.

Vandamme, N., Denecker, G., Bruneel, K., Blancke, G., Akay, Ö., Taminau, J., De Coninck, J., De Smedt, E., Skrypek, N., Van Loocke, W., et al. (2020). The EMT transcription factor ZEB2 promotes proliferation of primary and metastatic melanoma while suppressing an invasive, mesenchymal-like phenotype. Cancer Res. *80*, 2983-2995.

Williams, E.D., Gao, D., Redfern, A., and Thompson, E.W. (2019). Controversies around epithelial-mesenchymal plasticity in cancer metastasis. Nat. Rev. Cancer, *19*, 716-732.

Zhang, X., Xie, P., Zhang, K., and Zhang, W. (2023). Circulating tumour cell isolation, analysis and clinical application. Cell Oncol. (Dordr), *46*, 533-544.